

Draft: Acoustic resistance of can-annular combustor–turbine gaps

James Brind^a, Takaya Koda^b, Graham Pullan^a

^a *Whittle Laboratory, University of Cambridge,
1 JJ Thomson Avenue, Cambridge, CB3 0DY, UK*

^b *Research and Innovation Centre, Mitsubishi Heavy Industries,
2-1-1 Shinhamma Arai-Cho, Takasago, Hyogo 676-8686, Japan*

Abstract

We quantify acoustic resistance of the gap between a can-annular combustor and high-pressure turbine, using an experimentally validated time-marching computational approach. Adjacent cans oscillating in antiphase drive an unsteady flow through the combustor–turbine gap, creating a vortex sheet, dissipating acoustic energy, and affecting thermoacoustic stability. We use unsteady Reynolds-averaged Navier–Stokes simulations of two-can sectors to excite the antiphase mode and study two cases: a laboratory-scale experiment, and a realistic industrial gas turbine. Predictions of resistance for the validation case agree with measurements to a root-mean-square error of 8%, allowing for asymmetry of the real apparatus. Further results show linear dependence of quasi-steady resistance on through-gap bias and streamwise Mach numbers, with slope varying from 1.04 to 1.65 across gap lengths due to two-dimensional mean flow effects. In the industrial case, parametric studies of gap length and trailing edge thickness show resistance scales with a trailing-edge Strouhal number, and that vortex shedding is the dominant mechanism driving frequency trends. Approaching the characteristic Strouhal number of 0.2, vortex shedding acts as a source of acoustic energy and resistance falls to zero. By inhibiting vortex shedding, short gaps, vane clocking and coolant flow are shown to increase resistance at high frequencies by up to a factor of 5. Our findings demonstrate quantitative prediction of gap resistance, where existing analytical models fail, and provide design guidance on sensitivities to geometry and the underlying fluid dynamics in can-annular combustors.

Keywords: acoustic resistance, gas turbine, can-annular combustor

Nomenclature

Latin

a	Acoustic speed [m s^{-1}]
A	Area [m^2]
D	Trailing-edge thickness [m]
f	Frequency [Hz]
L	Gap length [m]
\dot{m}	Mass flow rate [kg s^{-1}]
n	Azimuthal mode number [-]
N	Number of combustor cans [-]
p	Pressure [Pa]
R	Vane leading-edge radius [m]
t	Time [s]
T	Temperature [K]
v	Velocity fluctuation [m s^{-1}]
V	Mean velocity [m s^{-1}]
W	Can width [m]

Greek

δ	Forcing amplitude [-]
γ	Ratio of specific heats [-]
η	Acoustic reactance [-]
ζ	Acoustic impedance [-]
ξ	Acoustic resistance [-]
ϕ	Forcing phase shift [rad]
ρ	Density [kg m^{-3}]

Dimensionless groups

Ma	Mach number, V/a [-]
St_D	Trailing-edge Strouhal number [-], Eqn. (9)
St_L	Gap Strouhal number [-], Eqn. (11)

Subscripts and accents

\pm	Adjacent can index
can	Can reference plane, Fig. 1
gap	Gap reference plane, Fig. 1

Abbreviations

TE	Trailing edge
URANS	Unsteady Reynolds-averaged Navier–Stokes

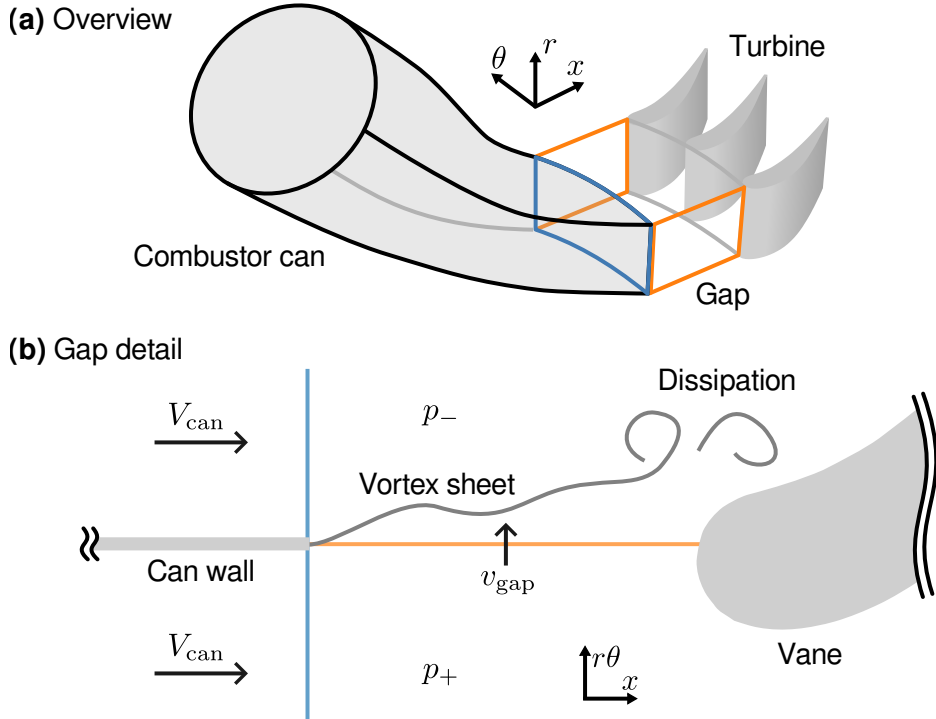


Figure 1: Combustor–turbine gap geometry: (a) overview of combustor can, axial gap, and turbine vanes; (b) mid-span detail view of gap area, with notation annotated.

1. Introduction

Can-annular combustors are composed of a ring of discrete combustion chambers connected to a downstream turbine via transition ducts, as illustrated in the overview of Fig. 1(a). Large industrial gas turbine manufacturers favour can-annular designs for their modularity, ease of maintenance, and for the ability to model near-field flame characteristics in a single-can configuration. Multiple cans do interact acoustically, however, through an open area or ‘gap’ between the combustor trailing edge and turbine leading edge [1].

The combustor–turbine gap gives rise to a mechanism of acoustic dissipation, not present in annular combustors, which is the subject of our paper. Prediction of dissipation levels in a combustor design is critical for thermoacoustic stability analysis. By the Rayleigh criterion, any in-phase pressure and heat release fluctuations act as a source of acoustic energy which must be balanced by propagation out of the domain, and dissipation within it, to maintain stability. Without sufficient damping, self-excited oscillations may grow to damaging levels [2].

It is convenient to model the oscillation of a ring of N combustor cans as a superposition of N azimuthal modes indexed over n [3]. When $n = 0$ all

cans oscillate in phase, an axisymmetric mode; when $n = N/2$ adjacent cans oscillate in antiphase, known as a ‘push-pull’ mode. Below a cut-off frequency, the axisymmetric mode transmits acoustic energy downstream, and our previous work on the reflection of plane waves by turbines provides methods to predict this effect [4]. In contrast, any non-axisymmetric mode with $n \neq 0$ drives an oscillatory flow through the combustor–turbine gap.

Existence of the $n = N/2$ push-pull mode in real can-annular combustors is well-supported by experimental data. Kaufmann et al. [1] compared measured pressure fluctuations in single-can and annular rigs, attributing an extra peak to a push-pull mode predicted by quarter-annulus computations. Venkatesan et al. [5], with a two-can test rig, showed that blocking the combustor–turbine gap eliminated a push-pull mode from their measurements. Moon et al. [6] found both push-pull and axisymmetric modes in a lab-scale rig, while Ghirardo et al. [7] identified push-pull and spinning $n = 2$ modes in engine data.

At an early design stage, computationally inexpensive low-fidelity network models allow faster exploration of the design space than high-fidelity computations. Network models incorporate the key influences of both the combustor–turbine gap, and the downstream turbine itself, as an impedance boundary condition applied at the combustor can trailing edge.

von Saldern et al. [8] developed a one-dimensional model for can-annular combustors, using the classical Rayleigh conductivity to relate pressure difference between adjacent cans to velocity through the gap. They assume a compact gap and an acoustically closed downstream turbine. Their result is a closed-form expression for effective reflection coefficient as a function of frequency, azimuthal mode number n , and can-to-gap area ratio. Fournier et al. [9] showed that two-dimensional effects necessitate an effective length correction if the von Saldern et al. [8] model is to match Helmholtz solver predictions. Orchini [10] derived a can-annular reflection coefficient including the additional effects of stream-wise mean flow and variable downstream turbine impedance.

All these analytical models take as empirical input the acoustic impedance of the combustor–turbine gap, which we define using the notation of Fig. 1(b) as,

$$\zeta = \xi + i\eta = \frac{1}{\rho a} \frac{p_+ - p_-}{v_{\text{gap}}}, \quad (1)$$

where $p_+ - p_-$ is the pressure difference between adjacent cans, v_{gap} is an unsteady acoustic velocity through the gap, and ρ and a are time-mean reference density and speed of sound respectively. The imaginary part $\text{Im}(\zeta) = \eta$ is acoustic reactance, corresponding to inertial effects; the real part $\text{Re}(\zeta) = \xi$ is acoustic resistance, quantifying dissipation. Henceforth, we drop the ‘acoustic’ qualifier and refer simply to impedance, resistance and reactance.

Brind [11] used unsteady Reynolds-averaged Navier–Stokes (URANS) computations of a large industrial gas turbine to validate the von Saldern et al. [8]

model. The results show that, in addition to an inertial Rayleigh conductivity, resistance is non-zero in real combustor–turbine gaps. A single fitted value of resistance is sufficient to match simulated can-to-can transfer functions for a range of can separations and gap lengths; the compact assumption of the analytical model, however, restricts validity of the analysis to low frequencies.

During preliminary design, when the details of the combustor and turbine geometry are not specified, it would be more valuable to predict resistance *a-priori* than to calibrate to three-dimensional simulations.

Howe et al. [12] presented a theoretical model for the resistance of an orifice in a zero-thickness plate subject to mean flow parallel to the plate. An oscillatory pressure difference across the orifice creates an unsteady vortex sheet along the dividing streamline, illustrated in Fig. 1(b), which must leave the plate smoothly to satisfy the Kutta condition. Assuming potential flow and enforcing continuity of pressure and displacement across the vortex sheet yields a solution for velocity, which is integrated to obtain orifice flow rate and hence impedance. The physical mechanism of acoustic dissipation is generation of vorticity by the imposed pressure difference; the vorticity is convected downstream and its kinetic energy eventually dissipated by viscosity (Fig. 1(b)).

Peat et al. [13] compared several extensions to the Howe et al. [12] model including the effects of finite plate thickness: Howe [14] and Jing et al. [15] for trailing edges much thinner than the gap length, and Howe [16] for trailing edges much thicker than the gap length. All analytical models predict no influence of plate thickness in the quasi-steady limit, but diverge at higher frequencies.

Where a time-mean pressure difference drives a bias flow through the orifice, according to the analysis of Howe [17], the physical mechanism of dissipation is similar. Flow separates as it exits the orifice, forming a vortex sheet; an oscillating pressure drop across the orifice modulates vortex sheet strength and sheds excess into the mean flow. Another commonality is that both bias and parallel flow theory predicts resistance to be directly proportional to Mach number [13].

Our aim in this paper is to quantify resistance of realistic combustor–turbine gaps, and assess sensitivities to geometry at compact and non-compact frequencies. Given the preponderance of the push-pull mode in reported measurements, we focus on the $n = N/2$ antiphase mode alone. We make the following contributions:

- An experimentally validated time-marching computational approach for predicting resistance of combustor–turbine gaps, compared against the laboratory-scale measurements of Blondé [18];
- Parametric studies quantifying the effects of streamwise and bias mean flow, can trailing-edge thickness, coolant flow, and gap length on combustor–turbine gap resistance in a representative industrial configuration; and

- Physical interpretation of the observed trends, with reference to flow field analyses and the accuracy of existing literature models for orifice impedance.

The remainder of this paper is structured as follows. Section 2 details our URANS simulation method and associated post processing. Section 3 presents validation of the computations against experimental data, and discusses the effects of mean flow and trailing edge thickness on resistance in a simplified geometry. Section 4 describes simulations of a realistic industrial gas turbine, presents further parametric studies, and explains the fluid dynamic mechanisms involved. Finally, Section 5 summarises our findings and conclusions.

2. Time-marching computational approach

This section outlines our approach to predicting the impedance of combustor–turbine gaps using time-marching computational fluid dynamics. We simulate a two-can sector of a can-annular combustor with antiphase acoustic excitation, and extract impedance from the resulting unsteady flow field. The section explains the boundary conditions, flow solver, and post-processing algorithms in turn.

2.1. Boundary conditions and acoustic excitation

The inlet boundary conditions are specified values of stagnation pressure, stagnation temperature, and flow angles. We prescribe zero swirl and pitch angles to fix the flow in the axial direction. The inlet boundary conditions are spatially uniform but functions of time. The outlet boundary condition is a constant and uniform static pressure.

To drive the antiphase mode of adjacent cans, we impose time-varying inlet boundary conditions at the upstream end of each can. Define a broadband sum of sinusoids forcing function,

$$F(t) = 1 + \sum_i \delta \sin(2\pi f_i t + \phi_i), \quad (2)$$

where $\delta \ll 1$ is a small amplitude, f_i are the excited frequency bins, and ϕ_i is a vector of phase shifts selected to minimise crest factor by a brute-force search over 500 random candidates. Negating δ excites the second can in antiphase. For isentropic forcing, the unsteady inlet boundary conditions are then,

$$\frac{p_{01}(t)}{\overline{p_{01}}} = F(t) \quad \text{and} \quad \frac{T_{01}(t)}{\overline{T_{01}}} = F(t)^{\frac{\gamma-1}{\gamma}}, \quad (3)$$

where p_{01} and T_{01} are inlet stagnation pressure and temperature, γ is the ratio of specific heats, and overbars denote time-mean values.

Our flow solver does not support characteristic non-reflecting boundary conditions, but this poses no practical problem. Reflections from the outlet boundary

are negligible at the combustor–turbine gap: the vanes are choked in the validation case; while the series of four high-subsonic turbine stages in the industrial case is also effectively choked. Reflections from the inlet boundary may be present, but Eqn. (1) remains valid locally at the gap irrespective of the details of the upstream wave field.

2.2. Flow solver

We use the TURBOSTREAM 3 GPU-accelerated flow solver for compressible URANS simulations [19]. The discretisation is second-order accurate in space using a finite-volume method on multi-block structured grids, and second-order accurate in time using implicit dual time stepping. Following previous acoustics studies with TURBOSTREAM [20, 4, 11], we select ample spatial resolutions of order 1000 points per shortest wavelength in the combustor–turbine gap, and use 72 time steps per shortest excitation period.

TURBOSTREAM uses a perfect gas equation of state and the Spalart–Allmaras turbulence closure. Assuming fully turbulent boundary layers, adaptive wall functions calculate the shear stress at solid boundaries.

The cases studied here have mesh sizes of 10–16 million nodes, and are run for 16 forcing cycles to ensure convergence of the acoustic response — one simulation requires up to 36 hours of wall-clock time on an Nvidia A100 GPU.

2.3. Post-processing to extract acoustic impedance

The solver outputs time histories of the flow field on sampling planes covering the can and gap cross sections, highlighted in Fig. 1(b). Our task is to extract can pressure difference and gap mass flow from these time histories to compute impedance using Eqn. (1).

The velocity v_{gap} through the gap is non-uniform, so we reformulate in terms of unsteady mass flow rate by taking v_{gap} to be the mass-averaged velocity over the gap cross section. Define

$$\dot{m}'_{\text{gap}} = \rho A_{\text{gap}} v_{\text{gap}} , \quad (4)$$

and eliminate v_{gap} from Eqn. (1),

$$\zeta = \frac{A_{\text{gap}}}{a} \frac{p_+ - p_-}{\dot{m}'_{\text{gap}}} . \quad (5)$$

Equation (5) is more convenient since it involves an integral quantity \dot{m}'_{gap} rather than a local velocity. The gap area A_{gap} is known from the geometry, while the acoustic speed a is time and area-averaged over the can cross section.

The unsteady mass flow rate is given by an area integral over the gap cross section at each time step,

$$\dot{m}_{\text{gap}}(t) = \int_{A_{\text{gap}}} \rho(t) \mathbf{V}(t) \cdot d\mathbf{A} . \quad (6)$$

We define the pressure difference between adjacent cans using area-averaged values over can cross sections A_{\pm} as,

$$p_{\pm}(t) = \frac{1}{A_{\text{can}}} \int_{A_{\pm}} p(t) dA . \quad (7)$$

We then take Fourier transforms of $p_+ - p_-$ and \dot{m}_{gap} to obtain their complex amplitudes as a function of frequency \hat{p} and \hat{m} , dropping the subscripts for clarity. To reduce noise at the expense of frequency resolution, we segment the time series into 7 segments with 50% overlap and apply a Hanning window. To reject uncorrelated noise, we compute the cross-spectrum between \hat{p} and \hat{m} and use this to evaluate impedance ζ as,

$$\zeta = \frac{A_{\text{can}}}{a} \frac{\sum_k \hat{p}_k \hat{m}_k^*}{\sum_k \hat{m}_k \hat{m}_k^*} , \quad (8)$$

where the sum is taken over segments k and asterisk denotes complex conjugate.

3. Experimental validation case

The primary aim of this section is to validate our computational approach against the experimental data by Blondé [18]. Further, we study the sensitivity of resistance to mean flow both parallel to and through the gap, and assess the accuracy of the Howe et al. [12] model for orifice impedance in this simple geometry.

Noting a lack of published experimental data on the resistance of combustor–turbine gaps, Blondé [18] presents measurements from a laboratory-scale model of an idealised gas turbine geometry. Figure 2 illustrates the apparatus: two square cross section ducts separated by a splitter plate, an adjustable-length gap, and three choked downstream vanes. Figure 2 also defines the relevant length scales: can width W , gap length L , and trailing edge (TE) thickness D . Although the geometry is idealised, the Mach, Strouhal and Helmholtz numbers match those of a real gas turbine. An upstream loudspeaker acoustically forces the upper duct, while a set of microphones records the pressure response in both ducts. Blondé [18] calculates impedance from a wave decomposition of the measured pressure fields in each duct.

The computational domain, Fig. 2, replicates the experimental geometry and time-averaged boundary conditions. As described in Section 2, we use unsteady

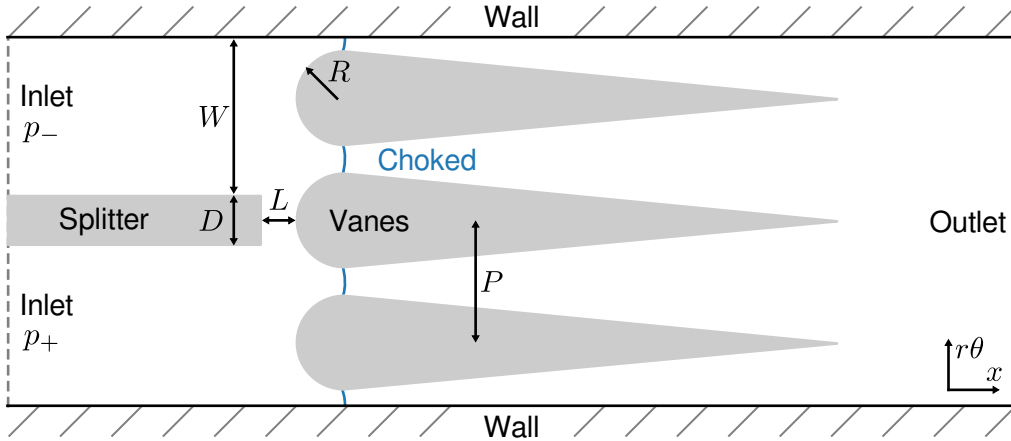


Figure 2: Domain and boundary conditions for Blondé [18] validation simulations. The geometry is two-dimensional into the page, with a radial span matching the experimental apparatus.

inlet boundary conditions to excite the antiphase mode, and calculate resistance from the resulting unsteady flow field. We select a forcing amplitude $\delta = 2 \times 10^{-4}$ in the linear regime. For the majority of simulations, we use a forcing frequency range corresponding to TE Strouhal numbers $0.008 \leq St_D \leq 0.08$ where,

$$St_D = \frac{fD}{V_{\text{can}}} , \quad (9)$$

and V_{can} is the upstream mean flow velocity in the can (Fig. 1(b)). For the validation case, we also run a second simulation with higher forcing frequencies $0.08 \leq St_D \leq 0.22$ to compare to the experimental data. The outlet boundary condition is a constant static pressure, which in this case is arbitrary as long as there is enough pressure drop to choke the vanes.

3.1. Comparison to measurements and sensitivity to gap bias flow

Figure 3 compares URANS predictions of resistance with the measurements for two gap lengths. For the 2D gap geometries considered in this paper, span may be divided out of the can-to-gap area ratio so that $A_{\text{gap}}/A_{\text{can}} = L/W$. The short gap has $L/W = 0.25$, while the long gap has $L/W = 0.45$.

We have scaled resistance by W/L to match the normalisation used by Blondé [18]. The data are plotted against a TE Strouhal number St_D , so that for these cases with constant TE thickness the horizontal axis is proportional to frequency. Hence, Fig. 3 may be directly compared to Fig. A.7 of Blondé [18].

We ran two separate simulations to cover the entire frequency range from approximately quasi-steady up to the first zero in the measured resistance data.

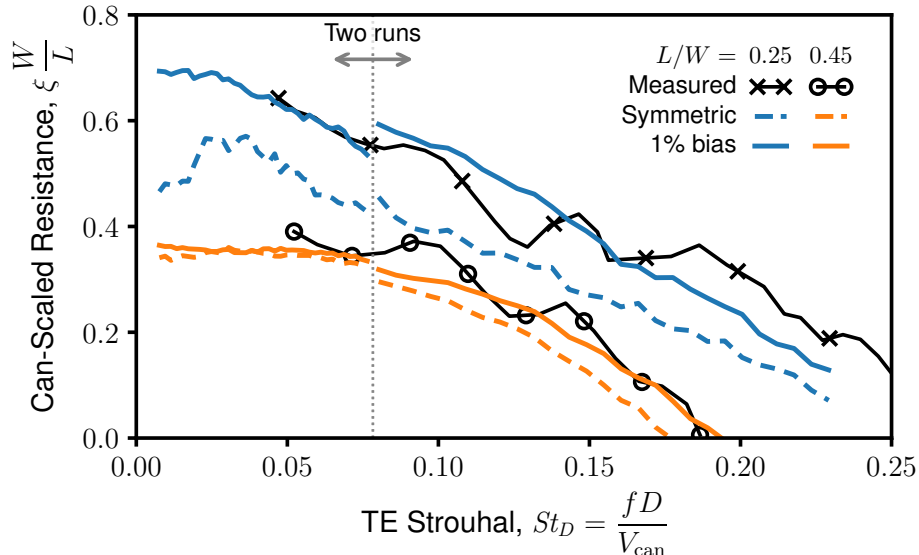


Figure 3: Validation of URANS-predicted acoustic resistance against Blondé [18] measurements. With 1% bias flow, equivalent to a 0.1 mm asymmetry in throat area, the predictions agree with measurements to an RMS error of 8%.

Where the results from both simulations meet at $St_D = 0.08$, there is a discontinuity in predicted resistance of up to 10% due to the change in temporal discretisation, although the runs are qualitatively consistent. In the following analysis, we focus on the lower frequency range $St_D \leq 0.08$ because the quasi-steady results are more interpretable, and, as the mesh is held constant, better resolved spatially.

Considering first the ideal symmetric geometry, dashed lines in Fig. 3, URANS under-predicts resistance by up to 24% at $L/W = 0.25$. We found the short-gap under prediction to be insensitive to spatial and temporal refinement, forcing amplitude, and turbulence model. Instead of numerical error, we attribute the discrepancy to asymmetry in the as-manufactured experimental apparatus.

In the experiment, upstream mass flow rates in each can are measured and set equal. The downstream mass flow rates through the vanes, however, are dictated by the choked condition. Any asymmetry in throat area will induce a bias flow through the gap to match the symmetry upstream, tending to increase resistance [17]. The total throat width is 11.4 mm, so a manufacturing tolerance of, say, 0.1 mm in positioning the central vane allows a 0.9% asymmetry in throat areas and hence bias mass flow through the gap of 0.9% \dot{m}_{can} .

To quantify the sensitivity of resistance to gap bias flow, we perform URANS simulations with increasing asymmetry in time-mean inlet stagnation pressure between the two cans (modifying the boundary conditions instead of geometry

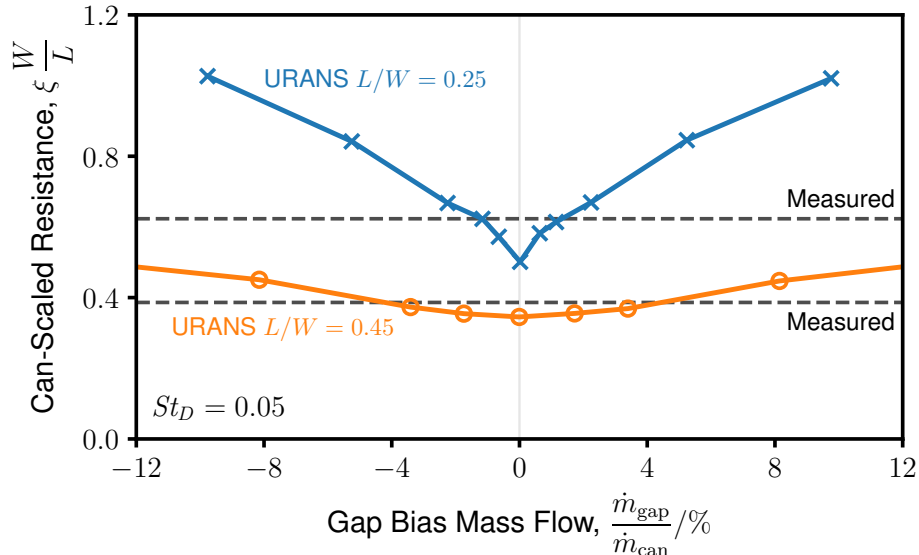


Figure 4: Sensitivity of URANS-predicted acoustic resistance to bias mass flow rate, at constant frequency $St_D = 0.05$, Blondé [18] case at two gap lengths. At $L/W = 0.25$, perfect symmetry under-predicts measurements by 20%, while a 1% asymmetry is sufficient to match experiments. At $L/W = 0.45$, the results are less sensitive to asymmetry, under-predicting by 8-12%.

for convenience). Solid lines in Fig. 3 show results for $\dot{m}_{\text{gap}}/\dot{m}_{\text{can}} = 1\%$ bias flow, which yield a closer match to the experimental data. Taking a root-mean-square (RMS) error over the entire frequency range, and normalising by the maximum measured resistance for each gap, 1% bias reduces RMS error from 19% to 7% for $L/W = 0.25$, and from 14% to 8% for $L/W = 0.45$.

Overall, Fig. 3 shows that our computational approach gives accurate predictions of both the quasi-steady value and frequency dependence of resistance, after allowing for a plausible asymmetry in the experimental apparatus.

Figure 4 displays resistance predictions over a range of bias flow rates from -12% to $+12\%$ \dot{m}_{can} at fixed frequency $St_D = 0.05$. The curves are symmetric about zero bias flow, with approximately linear dependence as predicted by analytical theory [17]. The $L/W = 0.25$ case appears more sensitive to bias flow, resistance increasing by a factor of 2.0 at $\dot{m}_{\text{gap}}/\dot{m}_{\text{can}} = 10\%$, compared to a factor of 1.4 for $L/W = 0.45$.

Figures 3 and 4 scale resistance by W/L , which increases apparent sensitivity for the short gap case with smaller L . Moreover, $\dot{m}_{\text{gap}}/\dot{m}_{\text{can}}$ alone is insufficient to characterise the flow through the gap, since for the same mass flow a smaller gap area implies a higher bias velocity. Figure 5 therefore re-plots the data of Fig. 4 with different variables that remove these first-order effects of gap area:

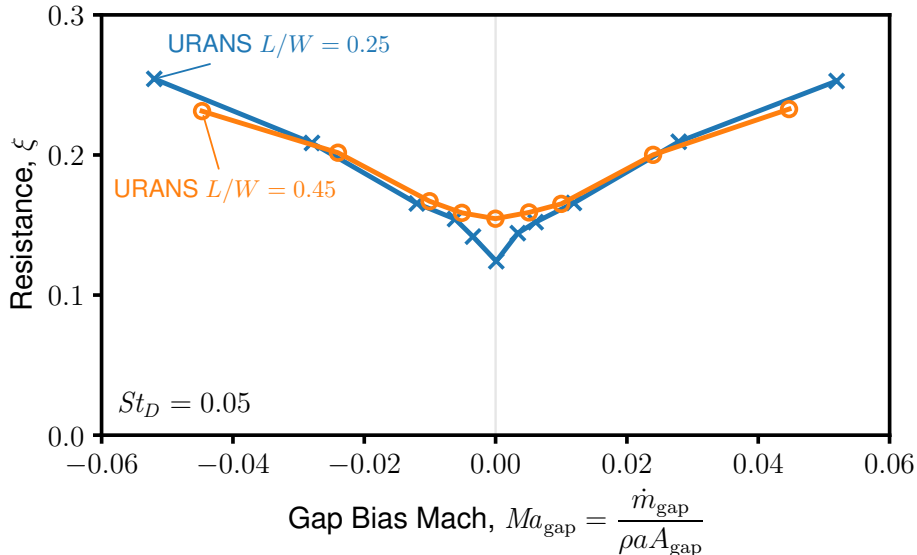


Figure 5: Sensitivity of URANS-predicted acoustic resistance to bias Mach number through the gap, at constant frequency $St_D = 0.05$. Blondé [18] case at two gap lengths. Both gap lengths collapse for higher bias Mach numbers, while differences of up to 24% remain for bias flows below $|Ma_{\text{gap}}| < 0.01$.

unscaled resistance ξ against an average bias flow Mach number,

$$Ma_{\text{gap}} = \frac{\dot{m}_{\text{gap}}}{\rho a A_{\text{gap}}}. \quad (10)$$

In Fig. 5, the curves for both gap lengths collapse towards each other, but residual differences remain for small asymmetry. In particular, the short gap resistance is 24% below the long gap resistance for perfect symmetry. We attribute the remaining difference to the fact that the short gap has a more non-uniform velocity field — a two-dimensional mean flow effect not captured by a simple gap-length scaling, which we elaborate on in the following Section 3.2.

3.2. Gap length and streamwise mean flow effects

The simple geometry and choked condition of the vanes in the Blondé [18] apparatus allows systematic computational study of the influence of streamwise mean flow on resistance. Keeping the upstream flow conditions fixed, because the vanes are choked the rig mass flow rate is directly proportional to vane throat area. We vary the vane leading-edge radius (R in Fig. 2) by up to 10% to adjust throat area and hence rig mass flow rate. This allows us to independently change the streamwise mean flow, Ma_{can} , and by a simple translation the gap length, L/W .

To explore the scalings and limitations of the Howe et al. [12] model for orifice impedance, we perform simulations with inviscid combustor walls and a thin TE, $D/W = 0$, in addition to the datum thick value of $D/W = 0.3$. Under the Howe et al. [12] assumptions, resistance is a function only of streamwise Mach number Ma_{can} and a gap length Strouhal number,

$$St_L = \frac{fL}{V_{\text{can}}} . \quad (11)$$

Figure 6 shows resistance predictions at a quasi-steady gap Strouhal $St_L = 0.02$ as a function of streamwise Mach number Ma_{can} for the thin TE case. Both the Howe et al. [12] model and the URANS computations show a linear dependence of resistance on Ma_{can} , although the analytical slope $d\xi/dMa_{\text{can}} = 1.13$ is 8% greater than the URANS slope $d\xi/dMa_{\text{can}} = 1.04$. Simulations for five gap lengths $0.22 \leq L/W \leq 0.39$ collapse to within $\pm 6\%$ resistance. Figure 6 demonstrates that, when the TE is thin, the direct influence of gap length on resistance is negligible if properly non-dimensionalised, and confirms the theoretical result that quasi-steady resistance is simply directly proportional to mean Mach number with a gradient of order unity. Figure 6 also supports validity of the computational approach — URANS predictions are consistent with the Howe et al. [12] analysis for a geometry that matches their modelling assumptions.

Figure 7 shows that for the thick TE case, the quasi-steady resistance slope is a function of gap length, unlike the thin TE case. The shortest gap $L/W = 0.25$ has a gradient $d\xi/dMa_{\text{can}} = 1.04$, below the Howe et al. [12] prediction; while the middle gap $L/W = 0.35$ has a gradient $d\xi/dMa_{\text{can}} = 1.65$, and the longest gap $L/W = 0.45$ has a gradient $d\xi/dMa_{\text{can}} = 1.29$. Published extensions to the Howe et al. [12] model for finite TE thickness do not predict any additional sensitivity in the quasi-steady limit when the TE thickness is much smaller than the acoustic wavelength [13], so we cannot account for the observed spread in Fig. 7 with existing analytical models.

The Howe et al. [12] model is inaccurate for thick TEs because these cases violate the assumptions of irrotational and uniform base flow. Figure 8 illustrates the real two-dimensional mean flow fields, predicted by URANS computations, using contours of time-averaged Mach number. For thin TEs, the top row of the plot, there is negligible influence on the mean flow as the gap length is varied. Due to the inviscid combustor wall, thin TEs have no boundary layers or flow separation. For thick TEs, the bottom row of Fig. 8, the flow field comprises a low-velocity recirculating separated region in the gap, divided from the mainstream by two shear layers. Longer gaps give more distance for the shear layers to grow; the shortest gap has an asymmetric field — these differences in mean flow field are the cause of sensitivity of resistance to gap length for thick TEs, not observed for thin TEs or captured by the Howe et al. [12] model.

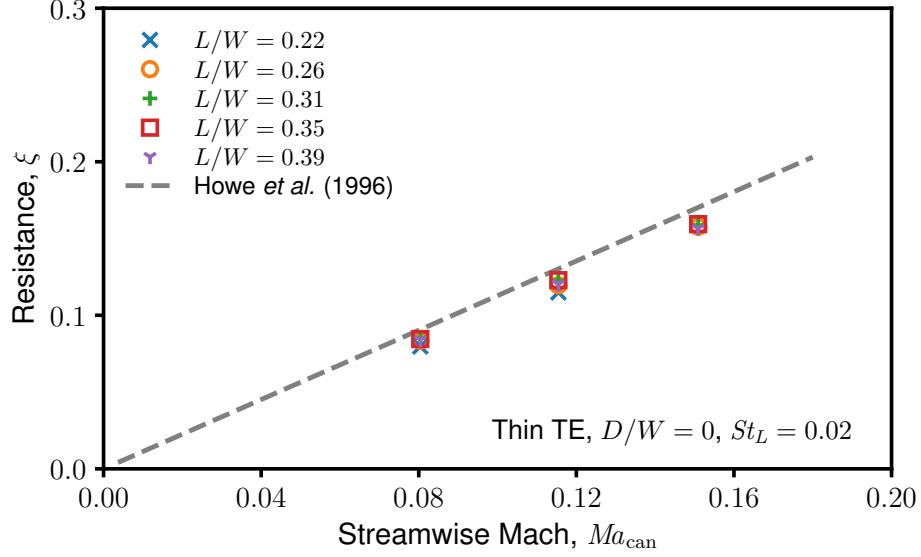


Figure 6: Acoustic resistance as a function of streamwise Mach number, for modified Blondé [18] geometry with thin TE $D/W = 0$, at gap Strouhal $St_L = 0.02$. The URANS and Howe et al. [12] predictions both show a linear dependence on Ma_{can} . Simulations for five gap lengths collapse to within $\pm 6\%$ resistance.

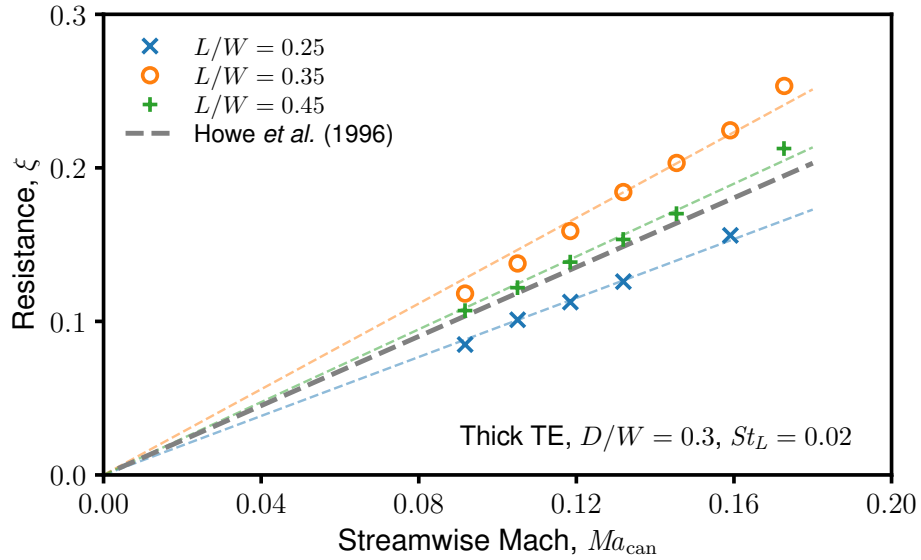


Figure 7: Acoustic resistance as a function of streamwise Mach number, for modified Blondé [18] geometry with thick TE $D/W = 0.3$, at gap Strouhal $St_L = 0.02$. Simulations predict the slope $d\xi/dMa_{can}$ is a function of gap length, the Howe et al. [12] model does not.

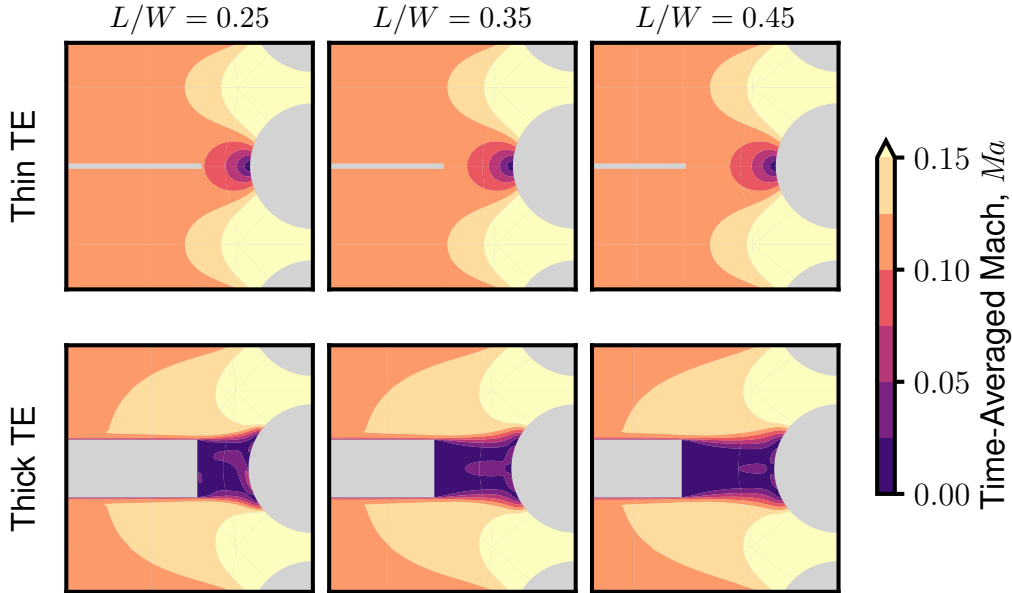


Figure 8: Time-averaged Mach number field predicted by URANS computations for the Blondé [18] geometry with thin and thick TEs, varying gap length at constant upstream $Ma_{\text{can}} = 0.12$. The mean flow is independent of gap length for the thin TE, but becomes a function of gap length for the thick TE.

We interpret the varying gradients $d\xi/dMa_{\text{can}}$ in Fig. 7 as changes in the effective streamwise velocity local to the gap. For a thin TE, following the Howe et al. [12] theory, the upstream Mach number alone is sufficient to characterise the convection of vorticity over the gap because the flow is approximately uniform. For a thick TE with a non-uniform velocity field and finite-thickness shear layers, the local velocity still scales proportional to the upstream Mach number but also depends on gap aspect ratio L/D via the 2D mean flow field.

We now consider trends of resistance with frequency. Figure 9 shows computations of resistance for the thin and thick TE cases with three gap lengths, varying gap Strouhal numbers $0.01 \leq St_L \leq 0.14$. The thin TE computations are almost independent of frequency over the studied range. The Howe et al. [12] model is more sensitive to frequency, moving from 17% over the simulations to 9% under as frequency increases. The thick TE results, however, depart from the analytical model by up to 45% and are not qualitatively consistent with the theory. Figure 9 suggests that the gap is not the length scale governing these frequency trends, especially with thick TEs. In the following Section 4, we will show that bluff-body vortex shedding, absent from the Howe et al. [12] model, is the mechanism responsible for the true frequency dependence.

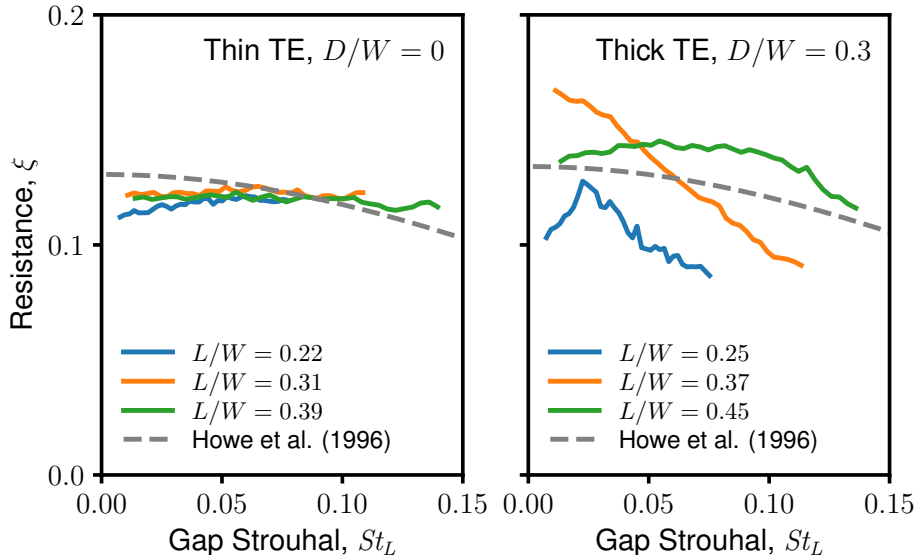


Figure 9: Predicted frequency trends of acoustic resistance for the Blondé [18] geometry with thin and thick TEs, varying gap length. For thin TEs, the resistance is independent of frequency; for thick TEs, gap Strouhal does not collapse the curves.

4. Gas turbine simulations

In this section, we describe the setup of our simulations of a large industrial gas turbine including the combustor–turbine gap, and present predictions quantifying the sensitivity of resistance to geometry in such a realistic configuration. We explain the fluid dynamics underlying the observed trends, with reference to the results presented in Section 3 for the simplified validation case.

Figure 10 illustrates the domain and boundary conditions for the gas turbine case. A can-annular combustor with square cross section cans is situated upstream of a four-stage axial turbine. There are 20 cans and 40 nozzle guide vanes, such that the vane pitch is half the can pitch. With the true combustor length, the quarter-wave mode lies inside the excitation frequency range; to avoid resonance contaminating the resistance predictions, we extend the can length by a factor of 10 as preliminary studies showed that results were independent of can length beyond this point.

The domain is periodic in the circumferential direction. The combustor and nozzle guide vanes are modelled in a two-can sector to capture the antiphase acoustic mode. We treat subsequent blade rows as single passages connected together with mixing planes that exchange circumferentially averaged flow quantities. Brind [4] showed that a single-passage turbine domain is sufficient to predict the reflections of plane waves incident from upstream, with an order of

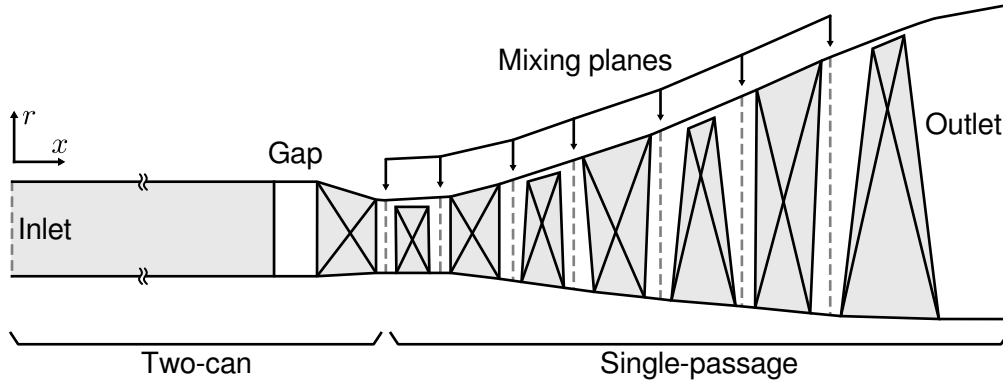


Figure 10: Domain and boundary conditions for industrial gas turbine simulations. The geometry is periodic in the circumferential direction, into the page for this meridional view. Combustor can length is not to scale.

magnitude reduction in computational cost compared to a two-can periodic sector for all blade rows. We model coolant flow added to the turbine and combustor by prescribing additional surface fluxes of mass, momentum, and energy.

As before, we use unsteady inlet boundary conditions to excite the antiphase can mode, setting forcing amplitude to a realistic level of $\delta = 1\%$. Compared to the validation case in Section 3, the higher amplitude here gives rise to non-linear effects and a dependence of predicted resistance on the stochastic forcing phases ϕ . We therefore report ensemble-averaged results over at least four simulations with different random seeds, together with 95% confidence intervals calculated using the Student’s t-distribution. This allows us to focus on systematic trends in resistance with geometry, rather than non-linear variability.

We present results from four parametric studies, each varying a single geometric parameter away from a datum case: gap length in Section 4.1; can trailing edge thickness in Section 4.2; combustor coolant flow rate in Section 4.3; and finally circumferential clocking of the vane with respect to the can in Section 4.3.

4.1. Gap length

Figure 11 shows the effect of gap length on resistance, in a format that will be used for subsequent parametric studies. The left-hand plot, Fig. 11(a), shows the quasi-steady resistance at a low Strouhal number $St_L = 0.02$ as a function of a design parameter, in this case gap length; the right-hand plot, Fig. 11(b), shows the frequency dependence of resistance for several points circled in the left-hand plot. The shaded regions denote confidence intervals for the ensemble-averaged resistance predictions, which are typically of order $\pm 5\%$ but vary between cases.

Figure 11(a) indicates that the Datum gap, $L/W = 0.15$, is a maxima in quasi-steady resistance: at $L/W = 0.06$ the resistance drops by 31%, while at

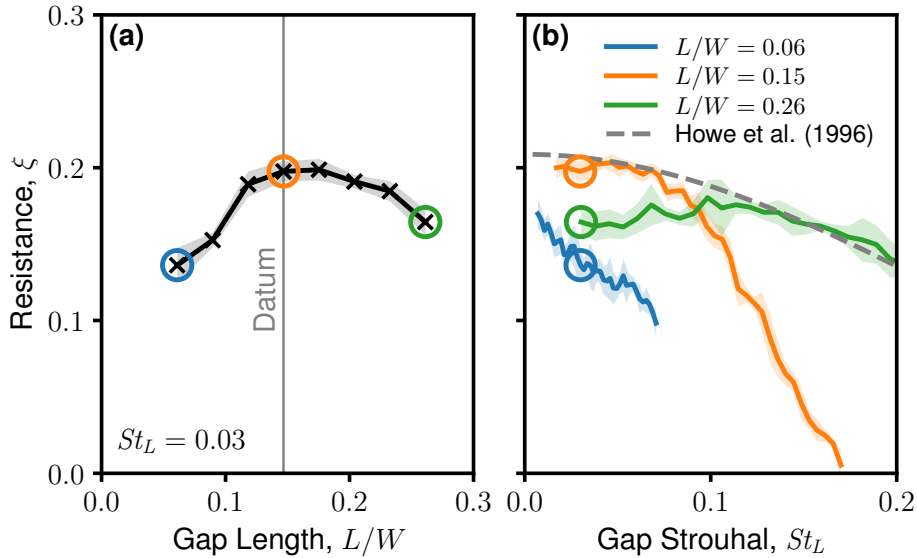


Figure 11: Effect of gap length on industrial gas turbine resistance, plotted against gap Strouhal St_L . The datum gap length is located at a maximum, with quasi-steady resistance values dropping by up to 31% for shorter gaps and 17% for longer gaps. The frequency trends are not collapsed by St_L , and do not match the Howe et al. [12] model.

$L/W = 0.26$ the resistance drops by 17%. This behaviour is qualitatively consistent with the Blondé [18] predictions in Fig. 7, which also show the greatest resistance at an intermediate gap length. Varying the gap geometry changes the effective streamwise velocity local to the gap, even when the upstream Mach number is fixed as in the gas turbine case.

The Howe et al. [12] model does not yield a good match to the URANS predictions in Fig. 11(b), failing to capture the quasi-steady effects or frequency trends. Like Fig. 9, the horizontal spread of the results when plotted against gap Strouhal St_L suggests that an alternative length scale might be more suitable. Hence, we plot Fig. 12 using TE Strouhal St_D instead. For these geometries with constant TE thickness, St_D is proportional to frequency (and independent of gap length).

The drop in resistance at $L/W = 0.06$ reduces to 17% when plotted at constant $St_D = 0.02$, but the qualitative trend in quasi-steady resistance is the same. The frequency curves in Fig. 12(b) are more closely aligned, and the longest two gaps approach zero resistance at the same St_D , confirming that the gap length scaling using St_L was counterproductive.

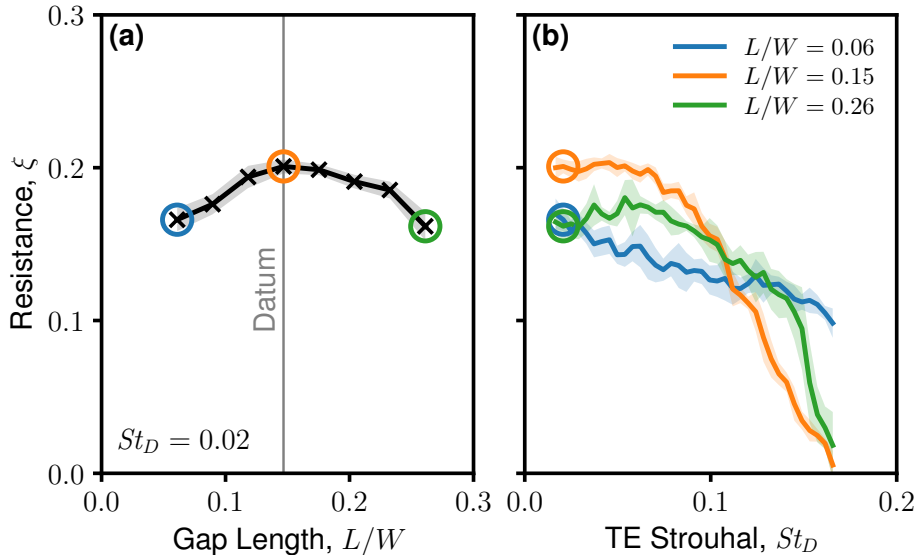


Figure 12: Effect of gap length on industrial gas turbine resistance, plotted against TE Strouhal St_D . The frequency curves collapse better than against St_D in Fig. 11(b).

4.2. Can trailing edge thickness

Figure 13 shows the sensitivity of acoustic resistance to five values of can trailing edge thickness $0.08 < D/W < 0.21$, with the datum case taking an intermediate value $D/W = 0.14$. The can pitch remains fixed, so increasing D reduces the available combustor width W ; we adjust the gap length by up to 6% to maintain a constant non-dimensional gap $L/W = 0.15$. Since the downstream mass flow rate is fixed by the turbine characteristic, the reduction in W also increases the can Mach number by up to 6%.

When plotted against gap Strouhal St_L , Fig. 13(a), the larger D/W cases show a steeper drop in resistance with frequency. Replotted against TE Strouhal St_D in Fig. 13(b), however, the middle three curves $0.11 \leq D/W \leq 0.18$ collapse to within the confidence intervals, while the thinnest and thickest edges also cluster towards the group. The collapse is direct evidence that, for sufficiently similar mean flows, TE thickness is the length scale governing the effect of frequency on resistance. On this basis, we use TE Strouhal number St_D for the horizontal axis in subsequent plots of frequency dependence.

At the Datum TE thickness $D/W = 0.14$, the top of the industrially representative forcing frequency range used for these simulations corresponds to $St_D = 0.17$, close to the characteristic frequency of bluff-body vortex shedding $St_D \approx 0.2$. At frequencies far below the shedding frequency, say $St_D \leq 0.05$, the resistance is approximately constant at the quasi-steady value. As the frequency approaches

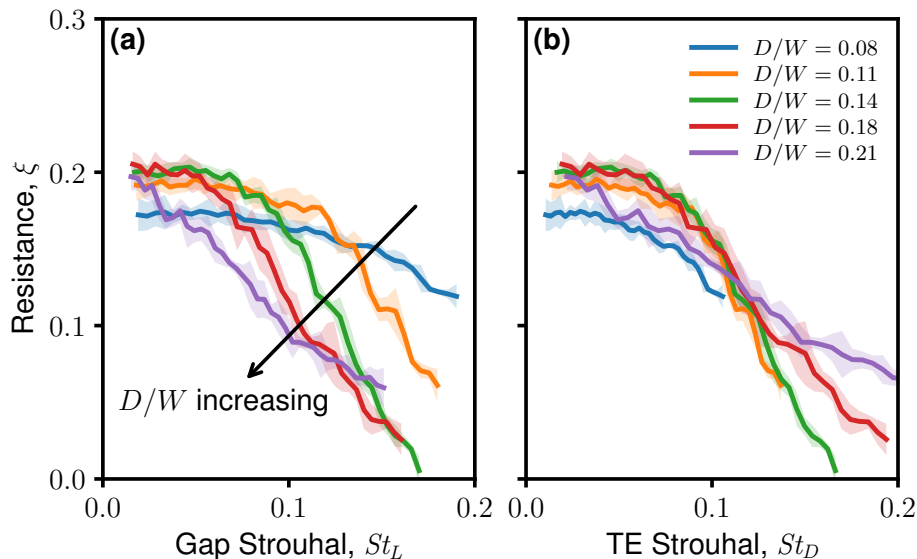


Figure 13: Sensitivity of URANS-predicted acoustic resistance to can TE thickness D/W , industrial gas turbine case. The curves for intermediate thicknesses collapse when plotted against TE Strouhal.

$St_D \approx 0.2$, resistance drops down to zero and will become negative at higher frequencies, because the vortex shedding acts as a source of acoustic energy.

The strong influence of vortex shedding in this problem has two key implications. First, being a non-linear, self-excited, double shear layer phenomenon, vortex shedding is not captured by the Howe et al. [12] model or amenable to an analytical treatment in general. Second, any design change that inhibits vortex shedding will increase resistance at high frequencies, potentially from a negligible positive or even negative value up to the order of the quasi-steady value. For example, returning to Fig. 12(b), the shortest gap $L/W = 0.06$ locates the vane too close to the can TE to allow a vortex street to form. At $St_D = 0.17$, the resistance is $\xi = 0.10$, compared to $\xi < 0.02$ for the longer gaps, a factor of 5 increase.

4.3. Combustor coolant flow

The datum case, for simplicity, neglects the real cooling flow added to control metal temperatures in the combustor. In practice, low-temperature air is injected throughout the combustor liner, but here we focus on the can TE as the location of most influence on the gap resistance.

We model coolant flow by injecting an axial flux uniformly over the can TE, with a stagnation temperature half that of the main stream, as shown by the flow field contours in Fig. 14. The coolant has several effects on the mean flow. First,

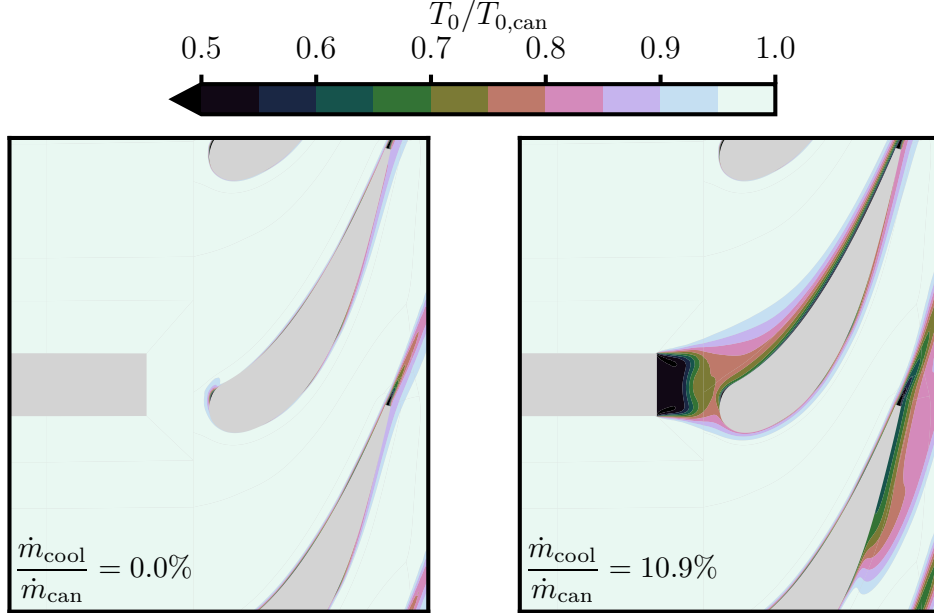


Figure 14: Contours of predicted time-averaged stagnation temperature at midspan for the industrial gas turbine simulations, with coolant flow injected at the can trailing edge.

because the turbine is effectively choked, the corrected mass flow rate through the vanes is fixed; adding coolant reduces the upstream mass flow and therefore the upstream can Mach number. Second, the temperature of the flow in the gap and hence the local speed of sound reduces. Finally, and most importantly, coolant injection increases the streamwise Mach number in the gap. Figure 15 shows the effect of these changes in mean flow on resistance. The geometry is held fixed, including the datum gap length $L/W = 0.15$.

For coolant mass flow fractions rates up to 5% inlet flow, at constant frequency $St_D = 0.02$, the effect on quasi-steady resistance is small and comparable to the shaded non-linear variability. The ensemble-averaged estimates in Fig. 15(a) do show, however, an upward trend with a resistance 17% above the datum at a coolant flow of $\dot{m}_{cool}/\dot{m}_{can} = 11\%$. We attribute the increase in quasi-steady resistance with coolant flow to an increase in local convection velocity over the gap, as discussed in Section 3.

The curves in Fig. 15(b) show that higher coolant flow rates yield a shallower drop in resistance as frequency increases. This is consistent with injection of coolant mitigating bluff-body separation behind the TE and hence suppressing vortex shedding. At $St_D = 0.17$, from essentially zero resistance without coolant flow, adding $\dot{m}_{cool}/\dot{m}_{can} = 11\%$ increases resistance up to $\xi = 0.15$.

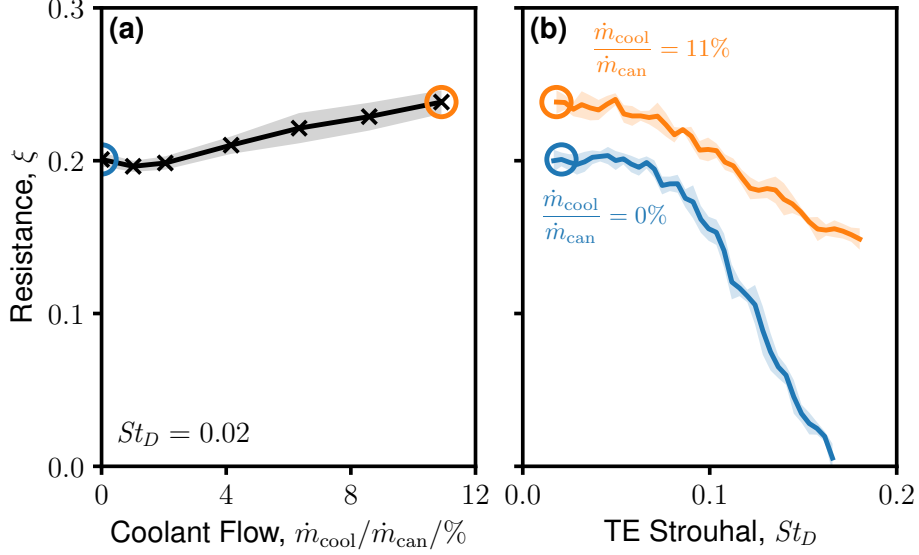


Figure 15: Sensitivity of URANS-predicted acoustic resistance to combustor coolant flow rate, industrial gas turbine case, at constant geometry. Resistance increases with coolant flow, due to increased Mach number in the gap and inhibited vortex shedding.

4.4. Vane clocking

‘Clocking’ refers to a circumferential offset of the turbine vane with respect to the combustor. Figure 16 shows how clocking affects the mean flow field in the gap: if can and vane are not aligned, high pressure at the vane stagnation point drives a bias flow through the gap in the circumferential direction. We would expect the strength of the clocking bias flow to reduce at longer gap lengths, or with reduced vane loading, as the potential field in the gap weakens.

From Section 3, resistance increases with bias flow magnitude and Fig. 17 confirms this mechanism is responsible for the sensitivity of resistance to clocking. Figure 17(a) plots resistance against bias Mach number, Eqn. (10), with tick marks at the corresponding clocking offsets showing a monotonic relationship.

By design, the datum clocking position has negligible bias flow, which Fig. 17(a) confirms has a minimum resistance. Moving away from the datum in either direction increases bias flow magnitude and hence resistance, by up to 71% at the quasi-steady Strouhal $St_D = 0.02$ when $\Delta r\theta/P = 0.1$.

Extracting frequency trends for the maximum and datum clocking positions in Fig. 17(b) shows that, in addition to a quasi-steady increase, the higher bias flow gives a shallower decrease in resistance with frequency. As with coolant ejection, superposing a mean bias flow through the gap disrupts bluff-body vortex shedding and hence the resistance remains positive at higher frequencies, whereas the datum position with negligible bias flow has zero resistance at $St_D = 0.17$.

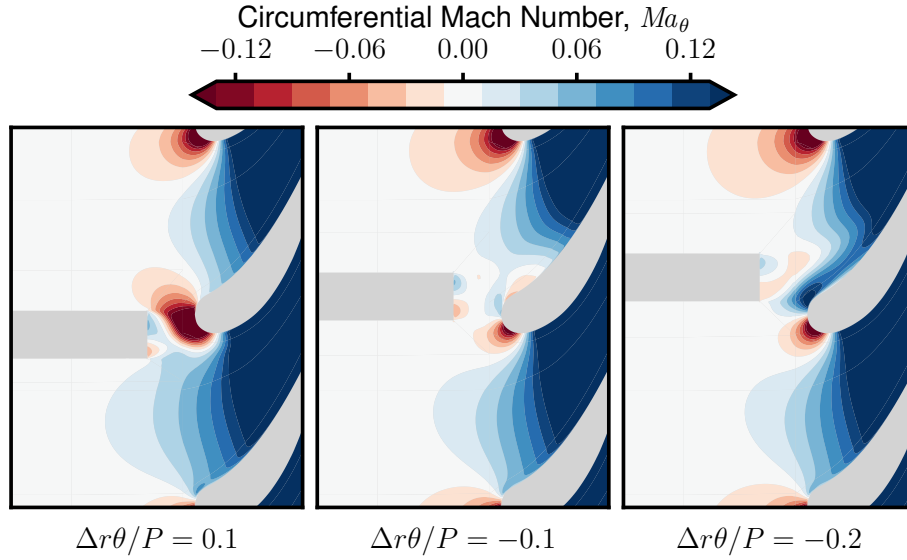


Figure 16: Contours of predicted time-averaged circumferential Mach number at midspan for different vane clocking offset, industrial gas turbine case. Positive offsets induce a negative bias flow through the gap, and vice versa.

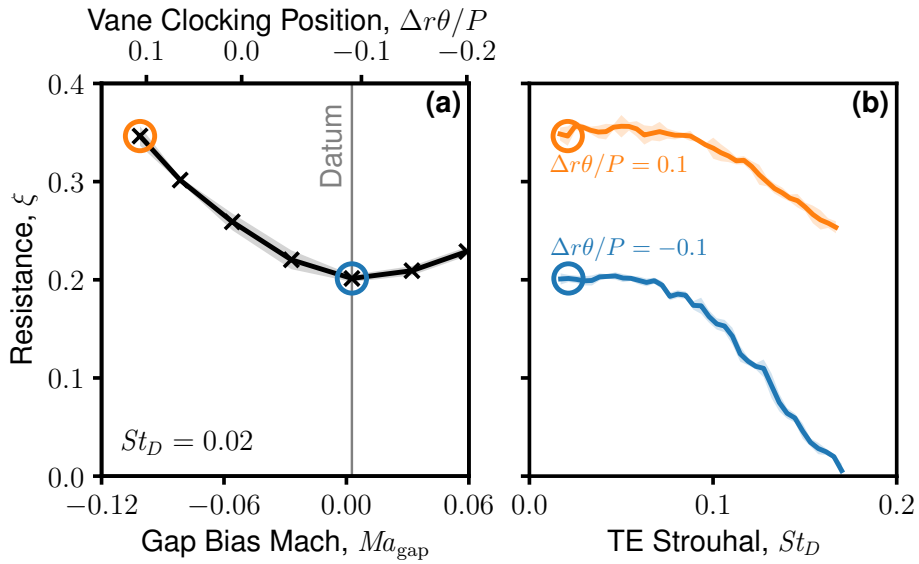


Figure 17: Sensitivity of URANS-predicted acoustic resistance to vane clocking offset, industrial gas turbine case. Resistance increases by up to 71% away from the datum position due to induced bias flow through the gap.

5. Conclusions

By performing URANS computations of two-can combustor sectors subject to antiphase acoustic forcing, we have quantified the sensitivity of combustor–turbine gap acoustic resistance to geometry and mean flow. The results support the following conclusions:

1. Our simulations of the Blondé [18] apparatus are accurate to a root-mean-square error of 8% with respect to the measured resistance. The results for the shortest gap exhibit a strong sensitivity to through-gap bias flow, so we allow for a 1% throat area asymmetry in the experimental apparatus.
2. Quasi-steady resistance is a function of a local streamwise velocity in the gap, which for thin trailing edges is simply the upstream can Mach number, but for practical thick trailing edges also depends on gap aspect ratio due to the non-uniform two-dimensional mean flow field.
3. Bias flow, whether induced by asymmetry in the experimental apparatus, or vane clocking in a real gas turbine, adds an extra quasi-steady resistance contribution of up to 71% in our studied cases.
4. Vortex shedding from the can trailing edge is the dominant mechanism responsible for frequency trends in resistance, as demonstrated by collapse when plotting against trailing-edge Strouhal number St_D . Vortex shedding acts as a source of acoustic energy and resistance drops to zero as frequency approaches $St_D \approx 0.2$. Bias flow, short gaps, and trailing-edge coolant injection mitigate vortex shedding, increasing resistance at higher frequencies.
5. Although the Howe et al. [12] analytical model is accurate to within 8% for zero-thickness trailing edges, when the trailing edge is thick the theory does not capture the influences of non-uniform mean flow on quasi-steady resistance, or frequency dependence due to vortex shedding.

Our work provides a validated computational approach for predicting gap resistance, guidance to combustor engineers on expected variations in acoustic dissipation due to design changes, and insight into the underlying fluid dynamic mechanisms.

6. Acknowledgements

The authors thank Mitsubishi Heavy Industries for funding this project under contract G532930, and for permitting publication of these results.

7. CRediT statement

JB: conceptualisation, methodology, software, investigation, writing; **TK**: conceptualisation, methodology, administration; **GP**: conceptualisation, supervision, review and editing, funding acquisition, administration.

References

- [1] P. Kaufmann, W. Krebs, R. Valdes, U. Wever, 3D Thermoacoustic Properties of Single Can and Multi Can Combustor Configurations, in: ASME Turbo Expo, 2008. doi:10.1115/GT2008-50755.
- [2] A. Dowling, The calculation of thermoacoustic oscillations, *J. Sound Vib.* 180 (4) (1995) 557–581. doi:10.1006/jsvi.1995.0100.
- [3] G. A. Mensah, G. Campa, J. P. Moeck, Efficient Computation of Thermoacoustic Modes in Industrial Annular Combustion Chambers Based on Bloch-Wave Theory, *J. Eng. Gas Turbines Power* 138 (8) (2016). doi:10.1115/1.4032335.
- [4] J. Brind, The acoustic impedance of three-dimensional turbines, *J. Sound Vib.* 541 (2022) 117311. doi:10.1016/j.jsv.2022.117311.
- [5] K. Venkatesan, A. Cross, C. Yoon, F. Han, S. Bethke, Heavy Duty Gas Turbine Combustion Dynamics Study Using a Two-Can Combustion System, in: ASME Turbo Expo, 2019. doi:10.1115/GT2019-90327.
- [6] K. Moon, H. Jegal, J. Gu, K. T. Kim, Combustion-acoustic interactions through cross-talk area between adjacent model gas turbine combustors, *Combust. Flame* 202 (2019) 405–416. doi:10.1016/j.combustflame.2019.01.027.
- [7] G. Ghirardo, C. Di Giovine, J. P. Moeck, M. R. Bothien, Thermoacoustics of Can-Annular Combustors, *J. Eng. Gas Turbines Power* 141 (1) (2019). doi:10.1115/1.4040743.
- [8] J. G. R. von Saldern, A. Orchini, J. P. Moeck, Analysis of Thermoacoustic Modes in Can-Annular Combustors Using Effective Bloch-Type Boundary Conditions, *J. Eng. Gas Turbines Power* 143 (7) (2021). doi:10.1115/1.4049162.
- [9] G. J. J. Fournier, M. Meindl, C. F. Silva, G. Ghirardo, M. R. Bothien, W. Polifke, Low-Order Modeling of Can-Annular Combustors, *J. Eng. Gas Turbines Power* 143 (12) (2021). doi:10.1115/1.4051954.
- [10] A. Orchini, An effective impedance for modelling the aeroacoustic coupling of ducts connected via apertures, *J. Sound Vib.* 520 (2022) 116622. doi:10.1016/j.jsv.2021.116622.
- [11] J. Brind, Acoustic boundary conditions for can-annular combustors, *Int. J. Turbomach. Propuls. Power* 8 (3) (2023) 32. doi:10.3390/ijtpp8030032.
- [12] M. Howe, M. Scott, S. Sipcic, The influence of tangential mean flow on the rayleigh conductivity of an aperture, *Proc. R. Soc. A* 452 (1953) (1996) 2303–2317. doi:10.1098/rspa.1996.0123.
- [13] K. Peat, R. Sugimoto, J. Horner, The effects of thickness on the impedance of a rectangular aperture in the presence of a grazing flow, *J. Sound Vib.* 292 (3–5) (2006) 610–625. doi:10.1016/j.jsv.2005.08.012.
- [14] M. Howe, Influence of wall thickness on rayleigh conductivity and flow-induced aperture tones, *J. Fluids Struct.* 11 (4) (1997) 351–366. doi:10.1006/jf1s.1997.0087.
- [15] X. Jing, X. Sun, J. Wu, K. Meng, Effect of grazing flow on the acoustic impedance of an orifice, *AIAA J.* 39 (8) (2001) 1478–1484. doi:10.2514/2.1498.
- [16] M. Howe, Low strouhal number instabilities of flow over apertures and wall cavities, *J. Acoust. Soc. Am.* 102 (2) (1997) 772–780. doi:10.1121/1.419903.
- [17] M. S. Howe, On the theory of unsteady high reynolds number flow through a circular aperture, *Proc. R. Soc. A* 366 (1725) (1979) 205–223. doi:10.1098/rspa.1979.0048.
- [18] A. Blondé, Thermoacoustic dynamics of gas turbine combustors: Effects of hydrogen blending and tunable acoustic boundaries, Ph.D. thesis (2023). doi:10.3929/ETHZ-B-000649708.
- [19] T. Brandvik, G. Pullan, An Accelerated 3D Navier–Stokes Solver for Flows in Turbomachines, *J. Turbomach.* 133 (2) (2011) 021025. doi:10.1115/1.4001192.
- [20] J. Brind, G. Pullan, Modelling Turbine Acoustic Impedance, *Int. J. Turbomach. Propuls. Power* 6 (2) (2021). doi:10.3390/ijtpp6020018.